

# Infrared measurements and simulations of metal meshes in a focused beam

K. P. Stewart,<sup>1,a)</sup> K. D. Möller,<sup>2</sup> and H. Grebel<sup>2</sup>

<sup>1</sup>Naval Research Laboratory, 4555 Overlook Avenue SW, Washington, DC 20375, USA

<sup>2</sup>Electrical Engineering Department, New Jersey Institute of Technology, Electronic Imaging Center, Newark, New Jersey 07102, USA

(Received 6 September 2013; accepted 27 January 2014; published online 6 February 2014)

Infrared transmittance measurements of quasioptical filters are often restricted to a focused beam due to the optical design of the spectrometer. In contrast, numerical simulations assume an incident plane wave, which makes it difficult to compare theory with experimental data. We compare transmittance measurements with numerical simulations of square arrays of circular holes in 3- $\mu\text{m}$  thick Cu sheets at angles of incidence from  $0^\circ$  to  $20^\circ$  for both  $s$  and  $p$  polarizations. These simple structures allow detailed tests of our electromagnetic simulation methods and show excellent agreement between theory and measurement. Measurements in a focused beam are accurately simulated by combining plane wave calculations over a range of angles that correspond to the focal ratio of the incident beam. Similar screens have been used as components of narrow bandpass filters for far-infrared astronomy, but these results show that the transmittance variations with angle of incidence and polarization limit their use to collimated beams at near normal incidence. The simulations are accurate enough to eliminate a costly trial-and-error approach to the design of more complex and useful quasioptical infrared filters and to predict their in-band performance and out-of-band blocking in focused beams. © 2014 AIP Publishing LLC.

[<http://dx.doi.org/10.1063/1.4864663>]

## I. INTRODUCTION

Periodic metal/dielectric structures have been used for spectral filter applications in the infrared to terahertz region for many years.<sup>1,2</sup> A study of metal screens with a rectangular periodic array of square-shaped apertures has been published in a forgoing paper,<sup>3</sup> and will now be extended to the angular and polarization dependence of metal screens with a rectangular array of circular apertures.

Filters for astrophysical and remote sensing applications are often designed by assuming incident plane waves, but tested in a spectrometer with a focused beam, and used in an instrument with yet another focal ratio. This can result in disagreement between predicted and measured optical properties and unexpected spectral features when used as a component of an astronomical sensor. It is possible to accurately predict the performance by averaging a series of plane wave simulations over a range of angles corresponding to the  $f$  number or cone angle of the instrument in which the filter will be used. We tested this averaging process by comparing the calculations with measurements of thin screens with circular holes arranged in a square array. Similar structures have been used as components of bandpass filters and as dichroic reflectors.<sup>4</sup>

Predicting the performance in a focused beam is important because improvements in background-limited detectors are rapidly moving far-infrared instrumentation to high throughput, large solid angle systems to improve sensitivity and mapping speed. It is necessary to control the light incident on the focal plane over a large range of angles, while simultaneously defining the spectral band. In order to capture the full

benefits of such design approaches, when implemented with quasioptical filters, the out-of-band response as a function of angle needs to be understood and controlled throughout the design and implementation process. Failure to account for filter response at large angles of incidence has required modifications to several astrophysics research instruments.<sup>5–7</sup>

At these submillimeter wavelengths, the structure can be thick enough to be freestanding, which eliminates the complications of dielectric substrates, and to prevent transmission through the metal film, but thin enough,  $t/\lambda \sim 0.03$ , to eliminate additional waveguide modes.<sup>8–10</sup>

## II. EXPERIMENT

Metal screens with circular holes in a rectangular array were made of Cu with high accuracy using commercial electroforming equipment. The periodicity of the array  $g = 100\ \mu\text{m}$ , the hole diameter  $d = 50\ \mu\text{m}$ , and nominal thickness  $t = 5\ \mu\text{m}$ . The actual thickness was measured with a Tencor Alpha-Step profilometer to be  $3\ \mu\text{m}$ , which is approximately 80 times the skin depth for Cu at a wavelength of  $100\ \mu\text{m}$ , assuming the bulk value of  $5.88 \times 10^{-8}\ \Omega\ \text{m}$  for the resistivity. A thickness of  $3\ \mu\text{m}$  was assumed in the numerical simulations. Fig. 1 is an image of the sample taken with a scanning electron microscope.

The transmission spectra were measured at a spectral resolution of  $\Delta\bar{\nu} = 1\ \text{cm}^{-1}$  in a vacuum FTIR spectrometer using a mercury arc source and a liquid-helium-cooled bolometer. The entrance aperture of the spectrometer was 12 mm. Despite not being a point source, calculations which assumed a single-mode plane wave incident on the sample agreed well with the measurements, as shown below. Because the beam in the sample chamber was focused, an

<sup>a)</sup>ken.stewart@nrl.navy.mil

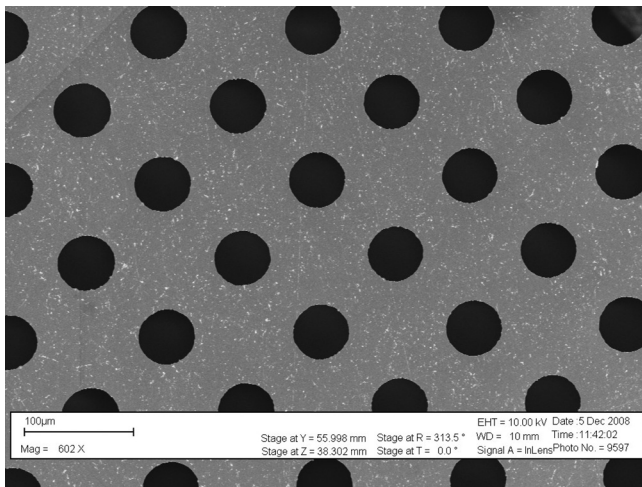


FIG. 1. SEM micrograph of the sample. The diameter of the holes is  $50\ \mu\text{m}$  and the periodicity is  $100\ \mu\text{m}$ .

iris was placed in front of the sample to limit the cone angle of the incident beam to more closely approximate the numerical simulations, which were restricted to incident plane waves. It was possible to reduce the cone angle to  $\sim \pm 2.4^\circ$ , while still maintaining adequate signal-to-noise ratio.

Two wire grid polarizers in series, placed in the incident beam before the sample, provided either a vertically or horizontally polarized beam on the sample. The grid spacing of the polarizers was  $25\ \mu\text{m}$ , so they were non-diffracting at the measured wavelengths ( $\lambda > 50\ \mu\text{m}$ ). In this spectral range, each polarizer transmitted less than 2% of the orthogonal component, giving  $< 0.04\%$  when both were used in series. The sample was rotated about a vertical axis to vary the angle of incidence as shown in Fig. 2. With this geometry  $s$  ( $p$ ) corresponds to vertical (horizontal) polarization.

The transmittance, measured in an  $f/12$  beam, for vertical polarization ( $s$ ) and horizontal polarization ( $p$ ), are shown in Figs. 3 and 4. The features below  $30\ \text{cm}^{-1}$  are noise caused by decreasing source intensity and beamsplitter efficiency. For  $s$  polarization, the electric field vector is perpendicular to the plane of incidence, parallel to the  $y$  axis of Fig. 2, about which the screen was rotated to vary the angle of incidence. The projection of the electric field vector in the plane of the sample is constant in magnitude and direction, independent of angle of incidence, and induces surface currents with wavelength almost independent of  $\theta$  (Fig. 3). For  $p$  polarization, the electric field vector is parallel to the plane of incidence. Its projection on the sample varies in magnitude with angle of incidence and induces surface currents along the  $x$  axis with a larger dependence on  $\theta$  (Fig. 4). The minima at slightly higher frequency than the peaks of the curves are due to Wood's anomaly,<sup>11,12</sup> where a diffracted mode is grazing the array. For the first order diffracted mode, these minima occur at  $\bar{\nu} = [g(\sin \theta + 1)]^{-1}$ , in agreement with the measured and calculated spectra. At higher frequencies, diffracted modes were scattered out of the beam of the spectrometer and did not reach the detector.

These results differ from the transmittance spectra of metal screens with square-shaped apertures, where the  $p$  component splits into two peaks.<sup>3,13</sup> The separation of the

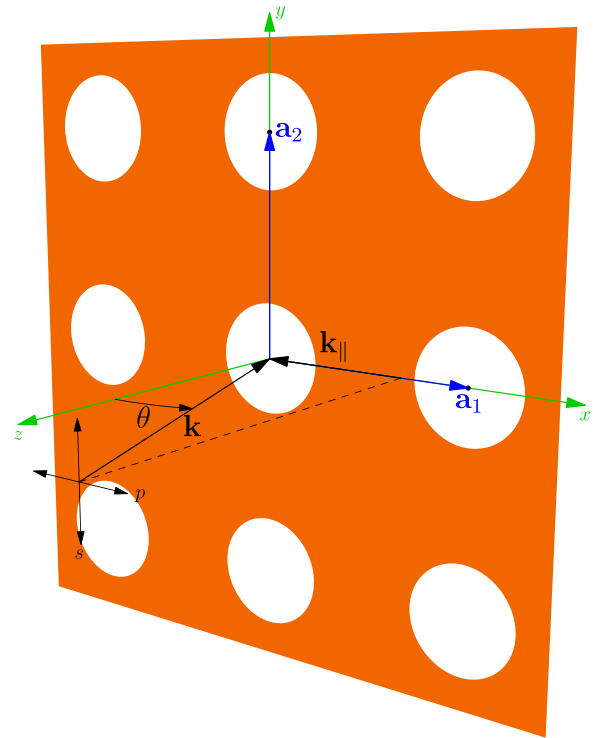


FIG. 2. Measurement geometry showing the wavevector  $\mathbf{k}$  at angle of incidence  $\theta$ . The lattice vectors  $|\mathbf{a}_1| = |\mathbf{a}_2| = g = 100\ \mu\text{m}$ . The diameter of the holes  $d = 50\ \mu\text{m}$ . The  $s$  (vertical) and  $p$  (horizontal) polarization directions are indicated.

peaks increases, the minimum broadens and shifts to lower frequency, as the angle of incidence increases and has been attributed to a photonic band gap.<sup>3</sup> The present results show only a single peak in the non-diffraction region ( $\lambda > g$ ). The sensitivity of the transmittance of this simple structure to angle of incidence limits its usefulness as an infrared filter to normal incidence in a nearly collimated beam.

### III. SIMULATIONS

#### A. Plane-wave calculations

Numerical simulations were performed using commercial finite-integral frequency-domain (FIFD) software (CST

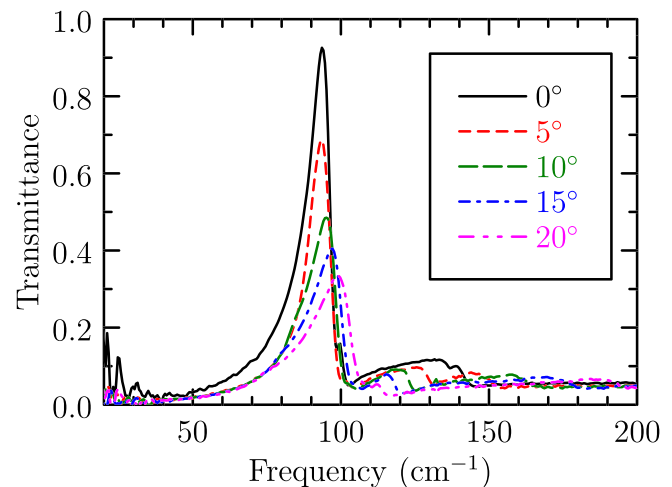


FIG. 3. Measured transmittance in an  $f/12$  beam, vertical ( $s$ ) polarization, at the indicated angles of incidence.

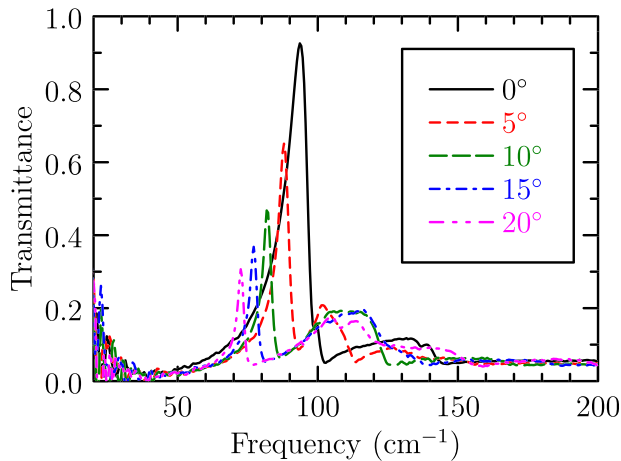


FIG. 4. Measured transmittance in an  $f/12$  beam, horizontal ( $p$ ) polarization, at the indicated angles of incidence.

Microwave Studio, version 2011.07) with incident plane waves. Periodic boundary conditions were used to simulate a two-dimensional infinite array of unit cells with the primitive lattice vectors  $\mathbf{a}_1$  and  $\mathbf{a}_2$  (Fig. 2). The angle of incidence was varied by introducing a phase shift of the incident plane wave across the periodic boundaries. Thus, there was a fixed phase relation between waves at different angles, and these simulations apply to the case of a telescope observing a spatially coherent astronomical point source focused through a mesh filter onto a detector. A full solution of the filter problem in a converging beam will need to quantify the effects of coherence among plane waves incident at different angles.

Figs. 5 and 6 show the calculated transmittance for plane waves at the indicated angles of incidence for transverse electric ( $TE_{00}$ ) and transverse magnetic ( $TM_{00}$ ) modes, respectively, assuming the bulk value of the resistivity and the measured thickness of  $3\text{ }\mu\text{m}$  for the Cu screen. The TE (TM) mode corresponds to  $s$  ( $p$ ) polarization in a collimated beam. At frequencies below  $200\text{ cm}^{-1}$ , 26 propagating Floquet modes are excited by this periodic structure. All of these modes are included in the calculation, but only the modes that are transmitted in the direction of the incident plane wave, are plotted in order to match the experimental

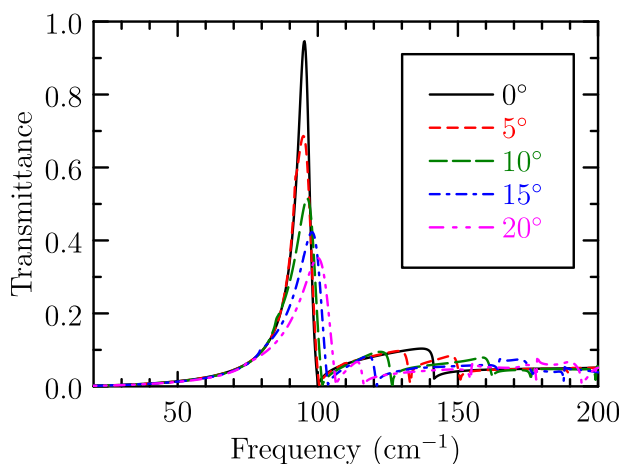


FIG. 5. Calculated transmittance for an incident plane wave, TE mode ( $s$  polarization), at the indicated angles of incidence.

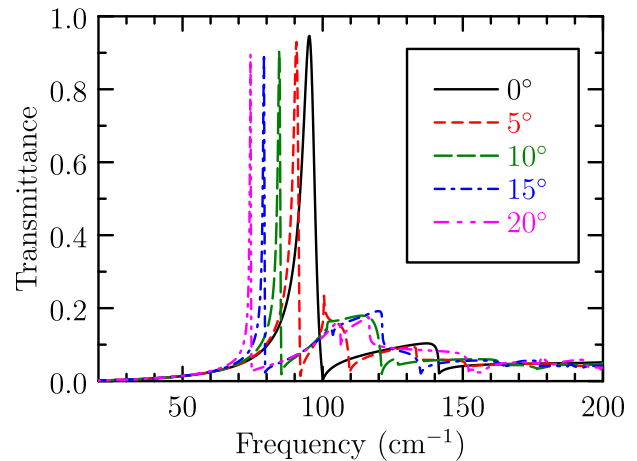


FIG. 6. Calculated transmittance for an incident plane wave, TM mode ( $p$  polarization), at the indicated angles of incidence.

conditions in which diffracted modes were scattered out of the spectrometer beam and did not reach the detector. The peak transmittance decreases rapidly and shifts to slightly higher frequency for the TE mode as the angle of incidence increases. The TM mode shows a smaller decrease in peak value, but a larger shift to lower frequency.

## B. Focused-beam calculations

At normal incidence, spectra of thin metallic sheets with an array of circular holes have a minimum transmittance at the wavelength  $\lambda = g$ , where  $g$  is the periodicity of the array,  $100\text{ }\mu\text{m}$  for these samples, and a sharp peak at slightly longer wavelength. The wavelength and amplitude of the transmittance peak shows a strong dependence on angle of incidence and polarization. This makes it difficult to compare theoretical simulations, which assume a collimated beam, with measurements, which were done in a focused beam due to the optical design of the spectrometer.

A focused beam can be modeled as a superposition of plane waves that cover the cone angle of the beam, centered on each angle of incidence. To simulate the focused  $f/12$  beam in the spectrometer, we calculated the transmittance at 17 angles in the horizontal and vertical directions  $\alpha$  and  $\theta'$ , respectively, shown in Fig. 7, around each angle of incidence and averaged the results. All of the angles were weighted equally; no attempt was made to simulate a Gaussian beam due to the unmeasured aberrations and small alignment errors in the optics of the spectrometer, and  $D \gg \lambda$ , where  $D = 50\text{ mm}$  is the diameter of the beam in the spectrometer and  $\lambda \sim 0.1\text{ mm}$ . We found this geometrical optics approximation to give excellent agreement between theory and experiment. This simulation method can be adapted to predict the performance of a quasioptical filter given the optical design of any instrument for which this approximation is valid.

For a collimated beam,  $\alpha = 0$ ,  $\theta' = \theta$ , and the TE (TM) mode is identical to  $s$  ( $p$ ) polarization or vertical (horizontal) direction for this measurement geometry. For a focused beam, rays are incident on the sample from directions out of the horizontal plane of incidence, the angles  $\theta'$  and  $\alpha$  are not

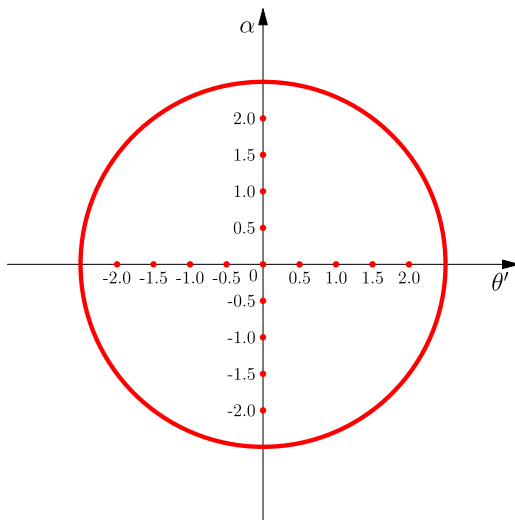


FIG. 7. The 17 points calculated for each angle of incidence, labeled in degrees. This range of angles corresponds to an  $f/12$  beam.

the same as the angles  $\theta$  and  $\phi$  in the spherical coordinate system with the  $z$  axis normal to the plane of the sample. We refer to the calculated modes as TE or TM to avoid confusion with the vertically or horizontally polarized measurements which, due to the focused beam, consist of a mixture of both modes. Fig. 8 shows the geometry of a ray that is out of the plane of incidence ( $\alpha > 0$ ) due to the focused spectrometer beam.

The cosine formula of spherical trigonometry gives for the spherical triangle PQR

$$\cos \alpha = \cos \theta \cos \theta' + \sin \theta \sin \theta' \cos R, \quad (1a)$$

$$\cos \theta = \cos \alpha \cos \theta' + \sin \alpha \sin \theta' \cos Q, \quad (1b)$$

where  $R = \phi$  is the angle between sides RP and RQ of the triangle,  $Q = 90^\circ$  is the angle between sides QR and QP of the triangle, and  $\alpha$ ,  $\theta$ , and  $\theta'$  are the angles subtended at the origin by sides QP, RP, and RQ of the triangle, respectively. Solving for  $\theta$  and  $\phi$  gives

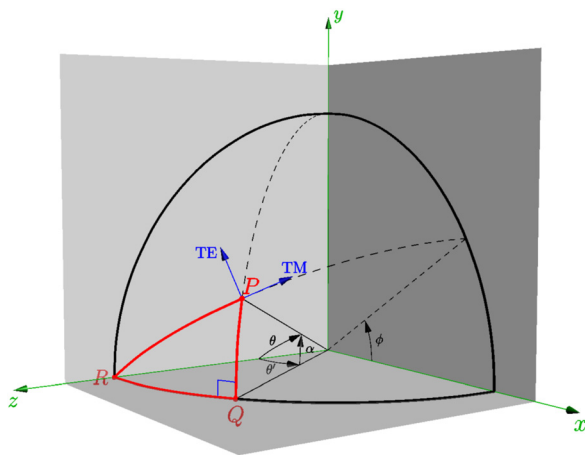


FIG. 8. The sample is in the  $x$ - $y$  plane with the direction of a ray incident from point P to the origin. For vertical ( $s$ ) polarization, the  $\mathbf{E}$  vector is parallel to the  $y$  axis, for horizontal ( $p$ ) polarization, it is parallel to the  $x$  axis. The TE and TM directions are indicated.

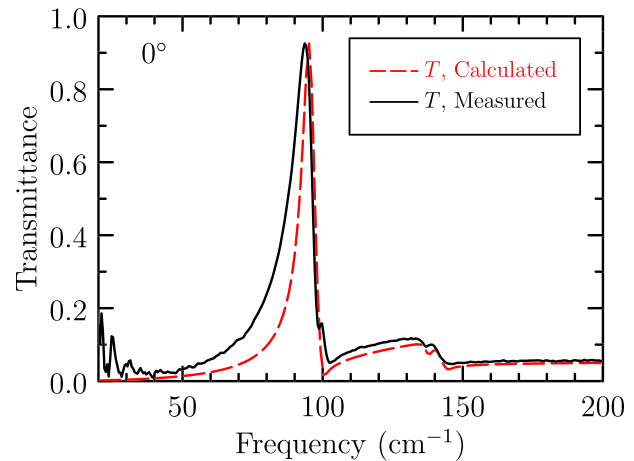


FIG. 9. Calculated (average over  $f/12$  beam) and measured transmittance for angle of incidence  $= 0^\circ$ . The vertical and horizontal components are degenerate at normal incidence.

$$\cos \theta = \cos \alpha \cos \theta', \quad (2)$$

$$\tan \phi = \frac{\tan \alpha}{\sin \theta'}. \quad (3)$$

The transmittance spectra  $T_v$  and  $T_h$  were measured with vertically and horizontally polarized beams. When  $\alpha \neq 0$  the calculated TE and TM modes are not aligned in these directions. The measured values must be calculated from

$$T_v = T_{TE} \cos^2 \phi + T_{TM} \sin^2 \phi, \quad (4a)$$

$$T_h = T_{TE} \sin^2 \phi + T_{TM} \cos^2 \phi. \quad (4b)$$

The plane-wave calculations look very different from the measurements, even with the incident beam in the spectrometer stopped down to  $f/12$ , due to the strong dependence of the transmission on the angle of incidence. Figs. 9–13 compare the focused-beam spectra, calculated as described above, with the measured spectra. The focused-beam calculations are in much closer agreement with the measurements than the plane-wave results. The peak frequencies are

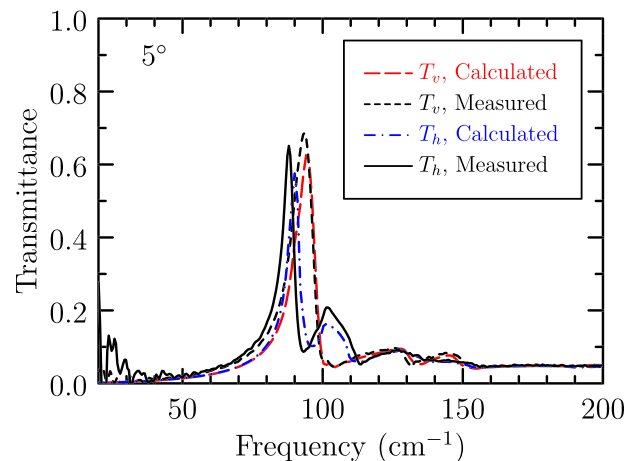


FIG. 10. Calculated (average over  $f/12$  beam) and measured transmittance for angle of incidence  $= 5^\circ$ .

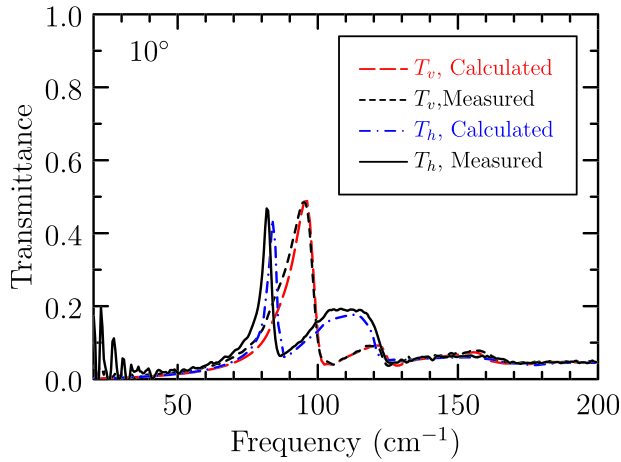


FIG. 11. Calculated (average over  $f/12$  beam) and measured transmittance for angle of incidence =  $10^\circ$ .

slightly better, but the peak transmittance values are much more accurate. Simulation of the diffraction region, important for controlling high-frequency leaks in astronomical instrumentation, is excellent.

The height of the peaks depends on the resistivity of the film. The accurate prediction indicates that the bulk Cu value is a good approximation. The calculated peaks are narrower than measured, as is most evident between  $60 \text{ cm}^{-1}$  and  $90 \text{ cm}^{-1}$  in Fig. 9 at normal incidence, but also visible at other angles of incidence. The widths of the peaks are sensitive to both the thickness of the film and the diameter of the holes. Although the spacing of the holes was very accurate, their diameter was observed to vary slightly and their edges had small irregularities ( $\sim 1 \mu\text{m}$ ). Assuming a larger effective diameter would improve the fit to the low-frequency side of the peaks. These fabrication errors contributed to this discrepancy.

#### IV. DISPERSION RELATION

Ref. 3 gave a one-dimensional analysis of the dispersion of square-hole samples in terms of surface waves (surface plasmon polaritons). Here, we summarize the results of the plane-wave calculations by presenting a more general

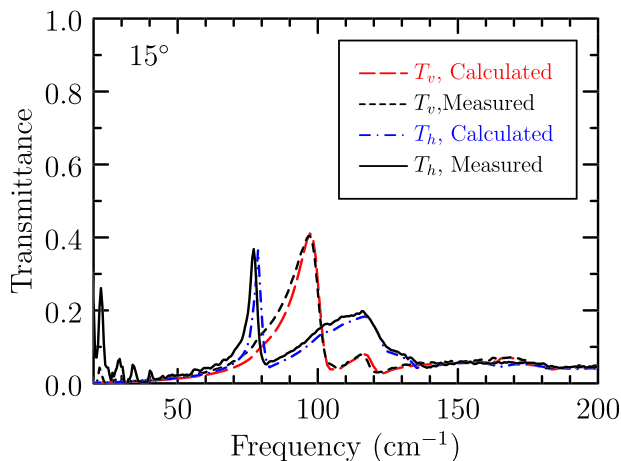


FIG. 12. Calculated (average over  $f/12$  beam) and measured transmittance for angle of incidence =  $15^\circ$ .

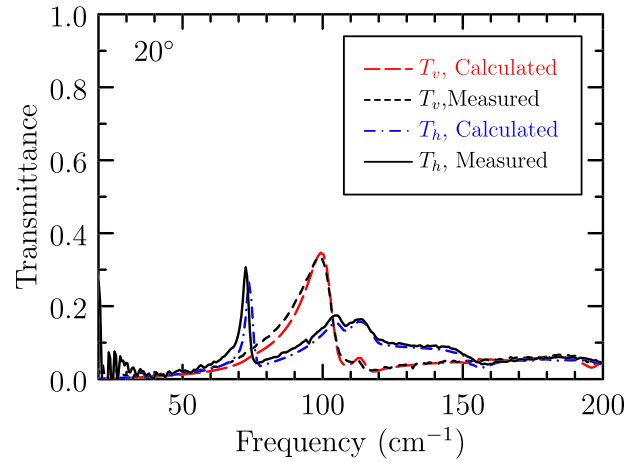


FIG. 13. Calculated (average over  $f/12$  beam) and measured transmittance for angle of incidence =  $20^\circ$ .

two-dimensional analysis that is applicable to structures with symmetries other than square, e.g., hexagonal.

The primitive vectors for the square mesh are  $\mathbf{a}_1 = g\hat{\mathbf{x}}$  and  $\mathbf{a}_2 = g\hat{\mathbf{y}}$ , where  $g$  is the periodicity of the lattice,  $100 \mu\text{m}$  for these samples (Fig. 2). The mesh is invariant under the translations  $\mathbf{T} = u\mathbf{a}_1 + v\mathbf{a}_2$ , where  $u$  and  $v$  are integers. The direct and reciprocal lattice vectors obey the orthogonality relations

$$\mathbf{a}_i \cdot \mathbf{b}_j = 2\pi\delta_{ij}. \quad (5)$$

This gives the primitive reciprocal lattice vectors

$$\mathbf{b}_1 = \frac{2\pi}{g}\hat{\mathbf{x}} \quad \text{and} \quad \mathbf{b}_2 = \frac{2\pi}{g}\hat{\mathbf{y}}. \quad (6)$$

A general reciprocal lattice vector is

$$\mathbf{G} = p\mathbf{b}_1 + q\mathbf{b}_2 = \frac{2\pi}{g}(p\hat{\mathbf{x}} + q\hat{\mathbf{y}}), \quad (7)$$

where  $p$  and  $q$  are integers.

The set of reciprocal lattice vectors  $\mathbf{G}$  determines the possible Bragg reflections. These occur when the incident and scattered wavevectors differ by a reciprocal lattice vector

$$\mathbf{k}' = \mathbf{k}_{\parallel} + \mathbf{G}, \quad (8)$$

where  $\mathbf{k}'$  is the scattered wavevector and  $\mathbf{k}_{\parallel} = \mathbf{k} \sin \theta$  is the projection of the incident wavevector in the plane of the sample

$$|\mathbf{k}'| = 2\pi\bar{\nu} = |\mathbf{k}_{\parallel} + \mathbf{G}| = \left| \left( k_{\parallel} + p\frac{2\pi}{g} \right) \hat{\mathbf{x}} + q\frac{2\pi}{g} \hat{\mathbf{y}} \right|, \quad (9)$$

where  $\bar{\nu} = 1/\lambda$  is the frequency of the scattered wavevector. Therefore

$$\bar{\nu}_{pq} = \pm \left[ \left( \frac{k_{\parallel}}{2\pi} + \frac{p}{g} \right)^2 + \left( \frac{q}{g} \right)^2 \right]^{1/2}, \quad (10)$$

with the sign chosen to give a positive frequency. The frequencies corresponding to the first few reciprocal lattice vectors are

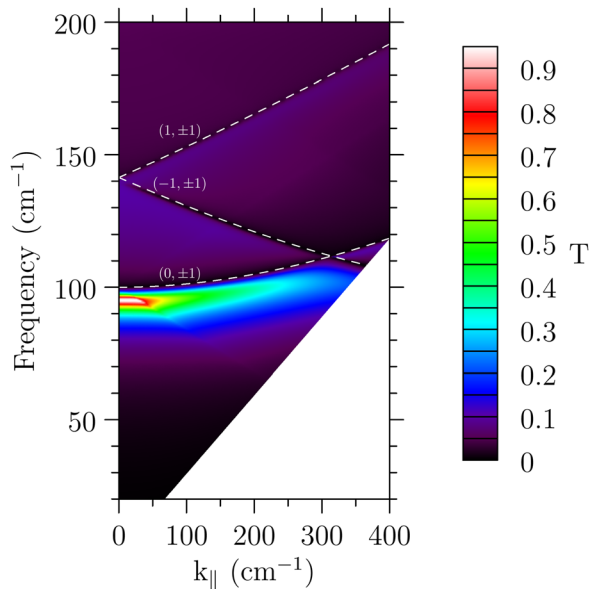


FIG. 14. Calculated dispersion diagram for the TE mode. The reciprocal lattice vectors responsible for the spectral features are labeled and plotted as dashed white lines. The Brillouin zone boundary is at  $\pi/g = 314 \text{ cm}^{-1}$ .

$$\bar{\nu}_{\pm 10} = \pm \frac{k_{||}}{2\pi} + \frac{1}{g}, \quad (11a)$$

$$\bar{\nu}_{0\pm 1} = \left[ \left( \frac{k_{||}}{2\pi} \right)^2 + \frac{1}{g^2} \right]^{1/2}, \quad (11b)$$

$$\bar{\nu}_{\pm 11} = \bar{\nu}_{\pm 1-1} = \left[ \left( \frac{k_{||} \pm \frac{1}{g}}{2\pi} \right)^2 + \frac{1}{g^2} \right]^{1/2}. \quad (11c)$$

Figs. 14 and 15 show the calculated transmittance data of Figs. 5 and 6, respectively, plotted as a function of frequency ( $\text{cm}^{-1}$ ) and the component of the incident wavevector

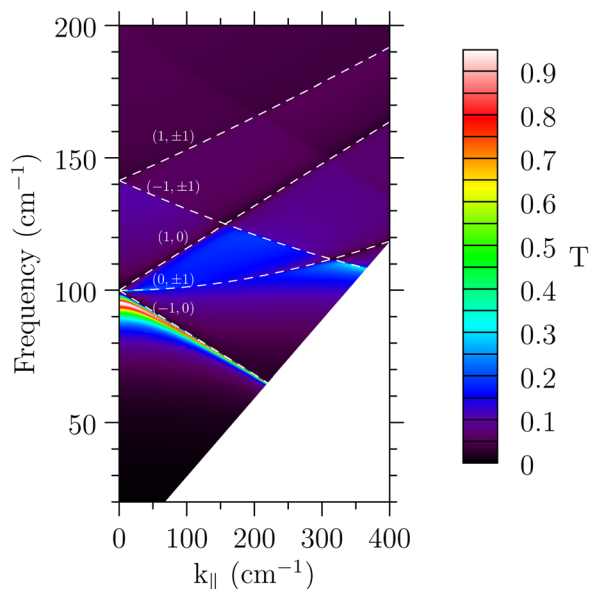


FIG. 15. Calculated dispersion diagram for the TM mode. The reciprocal lattice vectors responsible for the spectral features are labeled and plotted as dashed white lines. The Brillouin zone boundary is at  $\pi/g = 314 \text{ cm}^{-1}$ .

TABLE I. Modes  $(p, q)$  that appear in the dispersion graphs in order of increasing frequency. In each column, modes on the same line are degenerate.

TE	TM
$(0, -1) (0, 1)$	$(-1, 0)$
$(-1, -1) (-1, 1)$	$(0, -1) (0, 1)$
$(1, -1) (1, 1)$	$(1, 0)$
	$(-1, -1) (-1, 1)$
	$(1, -1) (1, 1)$

in the plane of the sample. The reciprocal lattice modes, Eqs. (11), indicated by the dashed white lines, match features in the spectra and are listed in Table I. The  $q = 0$  modes are not seen in the TE spectra.

## V. CONCLUSIONS

Transmission through a periodic array of circular holes is accurately described by numerical simulations averaged over a range of angles that correspond to the focal ratio of the incident beam. We have demonstrated quantitative agreement between theory and experiment for both polarizations at various angles of incidence. Because all propagating modes are calculated, any diffracted energy that is scattered into the transmitted beam by subsequent layers of multilayer filters would be included. This method can be used to predict and understand not only the in-band properties of quasioptical metal mesh filters, but also the high-frequency region, where diffraction from the periodic structures can cause unexpected leaks which, if not accounted for, can degrade instrument performance.

## ACKNOWLEDGMENTS

This material was based upon work supported by the National Aeronautics and Space Administration under Grant No. NNH08AI91I issued through the Science Mission Directorate.

<sup>1</sup>R. Ulrich, *Appl. Opt.* **7**, 1987 (1968).

<sup>2</sup>S. P. Varma and K. D. Möller, *Appl. Opt.* **8**, 1663 (1969).

<sup>3</sup>O. Sternberg, K. P. Stewart, Y. Hor, A. Bandyopadhyay, J. F. Federici, M. Bornfeld, Y.-L. Mathis, D. Sliwinski, K. D. Möller, and H. Grebel, *J. Appl. Phys.* **104**, 023103 (2008).

<sup>4</sup>T. Timusk and P. L. Richards, *Appl. Opt.* **20**, 1355 (1981).

<sup>5</sup>C. D. Dowell, C. A. Allen, S. Babu, M. M. Freund, M. B. Gardner, J. Groseth, M. Jhabvala, A. Kovacs, D. C. Lis, S. H. Moseley, T. G. Phillips, R. Silverberg, G. Voellmer, and H. Yoshida, *Proc. SPIE* **4855**, 73 (2003).

<sup>6</sup>E. H. Sharp, D. J. Benford, D. J. Fixsen, S. H. Moseley, J. G. Stagun, and E. J. Wollack, *Proc. SPIE* **8452**, 845231 (2012).

<sup>7</sup>P. Gallardo, R. Dünner, E. Wollack, F. Henriquez, and C. Jerez-Hanckes, *Proc. SPIE* **8452**, 845224 (2012).

<sup>8</sup>K. D. Möller, O. Sternberg, H. Grebel, and P. Lalanne, *J. Appl. Phys.* **91**, 9461 (2002).

<sup>9</sup>A. Roberts, M. L. von Bibra, H.-P. Gemünd, and E. Kreysa, *Int. J. Infrared Milli. Waves* **15**, 505 (1994).

<sup>10</sup>A. Lüker, H. Hein, J. Schulz, N. Dombrowsky, O. Sternberg, M. J. Sweetgall, K. Abdjalilov, K. D. Möller, and H. Grebel, *Infrared Phys. Technol.* **51**, 178 (2008).

<sup>11</sup>R. W. Wood, *Philos. Mag.* **4**, 396 (1902); *Phys. Rev.* **48**, 928 (1935).

<sup>12</sup>A. Hessel and A. A. Oliner, *Appl. Opt.* **4**, 1275 (1965).

<sup>13</sup>H. M. Pickett, J. Farhoomand, and A. E. Chiou, *Appl. Opt.* **23**, 4228 (1984).